Small Structures

small structures

www.small-structures.com

RESEARCH ARTICLE OPEN ACCESS

Structural Engineering of Reversible Hydrogel Nanocomposites for Dehydration-Free and Highly Durable Wearable Sensing Arrays

Animesh Sinha[1] | Minjoon Kim[2] | Hongyun So[1,2,3]

[1]Department of Mechanical Convergence Engineering, Hanyang University, Seoul, Republic of Korea | [2]Department of Semiconductor Engineering, Hanyang University, Seoul, Republic of Korea | [3]Institute of Nano Science and Technology, Hanyang University, Seoul, Republic of Korea

Correspondence: Hongyun So (hyso@hanyang.ac.kr)

Received: 6 July 2026 | **Revised:** 1 September 2026 | **Accepted:** 10 September 2026

Keywords: fatigue resistance | high fracture toughness | humectant-modified gel | hybrid conductivity | multipoint sensor

ABSTRACT

Hydrogels consist of crosslinked polymer chains that can hold substantial water within their 3D architectures. Nevertheless, most of this water exists in an unbound state, rendering progressive dehydration an inherent limitation that undermines fracture toughness and long-term fatigue durability. Although PVA/glycerol binary systems have been extensively investigated to address dehydration, they consistently entail a critical trade-off either exhibiting low mechanical stiffness or lacking quantified fatigue thresholds, fundamentally limiting their long-term wearable reliability. We demonstrate that suppressing dehydration through precise humectant engineering directly enhances mechanical durability. In this study, we designed interlinked structures using enhanced intermolecular association and dense networks enabled by dynamic plasticization-controlled chain mobility. We also observed that, after 7 days of dehydration, the hydrogel with a hybrid conductive network via optimal polymerization and the incorporation of functional additives led to high ultimate tensile strength (~2131 kPa), modulus (~685 kPa), fracture toughness (~3365 J/m^2), and fatigue threshold (~183 J/m^2), and an excellent gauge factor of 1.66 in the strain range of 100%–200%. These results establish a new performance benchmark for fatigue-resistant hydrogel sensors in wearable and flexible electronics. Durable, conductive hydrogels will improve clinical monitoring devices and advanced soft robots, thereby modernizing healthcare and automation.

1 | Introduction

A basic polymer matrix requires good tensile strength, modulus, maximum elongation, fracture behavior, and fatigue resistance as crucial mechanical attributes [1–3]. On the other hand, flexibility, stretchability, strength, and long-term stability are the main parameters that current flexible electronic applications require [4, 5]. Hydrogels have recently gained prominence for use in several scenarios, including in human motion sensors [6], actuators [7], and soft robotics [8], as well as flexible electronic [9], artificial tissue [10], and healthcare [11] applications. Nevertheless, how the water content impacts the fundamental features of a hydrogel, particularly its mechanical behavior, is of considerable importance across all of the abovementioned applications. Recent research findings have revealed that hydrogels composed of polyacrylamide (PAAM) or polyvinyl alcohol (PVA), which are the most frequently used types, continue to confront issues related to freezing and thawing, leading to prolonged curing times [12–18], poor long-term stabilities [19–22], structural failure [17], and sensing characteristics that degrade over time [23].

Specific methodologies have been established for effectively inhibiting fatigue cracks and enhancing the fracture toughness and fatigue threshold of a hydrogel, which are closely related to its

This is an open access article under the terms of the Creative Commons Attribution License, which permits use, distribution and reproduction in any medium, provided the original work is properly cited.

© 2026 The Author(s). *Small Structures* published by Wiley-VCH GmbH.

durability and structural collapse. Zhang et al. reported that the PAAM-based hydrogel model exhibits near-elasticity at the macroscopic level, thereby serving as the principal network in a resilient hydrogel, with a maximum fatigue threshold of 64.5 J/m^2 and a fracture energy of 611 J/m^2 [24]. Similarly, Sun et al. investigated high-aspect-ratio nanofibers within an elastic hydrogel matrix and reported that significant toughness (1000 J/m^2) and fatigue resistance (100 J/m^2) are achieved through reversible fiber alignment [25]. Hydrogels with anti-fatigue properties and high fracture toughnesses present major long-term application challenges but are essential developmental objectives. Most toughening strategies focus on endowing hydrogels with energy-dissipating mechanisms; however, these approaches often do not yield substantial increases in the fatigue threshold. Lei and coworkers examined the use of polyprotein crosslinkers to inhibit crack propagation, resulting in a hydrogel with high fatigue endurance [26]. Recent advances in the development of fatigue-resistant robust hydrogels have significantly expanded their application in sensing technologies. Structural engineering approaches, such as directional freeze-casting combined with thermal annealing or salting-out, have produced anisotropic, hierarchically aligned PVA and PEDOT:PSS-PVA hydrogels with high fatigue thresholds and effective crack-pinning properties [27, 28]. Additionally, advanced manufacturing techniques, including 3D printing of microphase semi-separated networks and electrical bioadhesives, have facilitated the creation of highly stretchable sensors exhibiting ultralow hysteresis and strong tissue adhesion [29, 30]. To address the challenge of long-term environmental stability, binary solvent systems containing glycerol have been used to fabricate anti-dehydration organohydrogels with exceptional stretchability, suitable for continuous monitoring [31]. Recent developments in conductive hydrogels have broadened their use in wearable and bioelectronic systems by improving charge transfer, mechanical flexibility, interfacial durability, signal reliability, and environmental resilience. Researchers have developed numerous hydrogel systems for neural and bioelectronic interface design, physiological signal monitoring, and mechanically adaptable sensing, highlighting the need to simultaneously control electrical conductivity, mechanical properties, and interfacial performance for reliable wearable technologies [32–35].

Furthermore, Liu et al. established a mechanism by which chemical crosslinkers relax fracture tips [36]. Kim et al. reported that chain entanglement is potentially more advantageous than a cross-linked polymeric framework [37] and asserted that stress propagates along the chain and to several additional strands via entanglements when the polymer is stretched, which enhances its toughness. The fracture durabilities and fatigue thresholds of organogels, which differ from conventional hydrogels, have recently been examined by aligning nanowires to form anisotropic architectures [38]. However, this technique involves lengthy and complex synthesis processes, intricate designs, and inhomogeneous structures, which limit its practicability. Therefore, developing highly tough hydrogels that retain their properties over time remains challenging.

Herein, we comprehensively analyze mechanical behavior in relation to solvent composition and hydration kinetics. Furthermore, deformation-dependent electromechanical properties were examined by assessing cycling stability and the fatigue threshold. Our investigation encompassed the development of fatigue-resistant hydrogels and aimed to comprehend their underlying mechanisms by preparing three distinct PVA-based hydrogels: 1) PVA/DI water, 2) PVA/ethylene glycol (EG), and 3) PVA/glycerol (G). Design strategies that produce robust hydrogels were subsequently implemented; these strategies included optimizing polymer concentration and crosslinking density, which are crucial for enhancing hydrogel durability and performance under various conditions. Additionally, PVA/glycerol hydrogels with varying glycerol contents and integrated with functional additives (i.e., LiCl, PEDOT:PSS, and COOH-CNT) were synthesized and used in multipoint human–muscle movement applications. The experimental results reveal that the PVA/G-based hydrogel is endowed with a tensile strength and modulus that are ~126% and ~327% higher, respectively, than those of the PVA/EG hydrogel and ~626% and ~2622% higher, respectively, than those of the PVA/water-based hydrogel. Electromechanical testing revealed a gauge factor (GF) of ~1.66 in the strain range of 100%–200% and a reaction time of approximately 250 ms. These findings highlight the potential of hydrogel as a sensitive and stable strain sensor for monitoring muscle movement in the human forearm during flexion. In summary, this study developed an innovative technique for producing reliable hydrogels for use in flexible electronic applications that include multifunctional mechanisms, such as sophisticated sensors and wearable devices.

2 | Experimental Section

2.1 | Materials

PVA with an average molecular weight (MW) of 120,000 was obtained from Thermo Fisher Scientific. Lithium chloride (LiCl), known for its high solubility and good ionic conductivity (≥99.98% trace metals basis) and PEDOT:PSS (dynamic viscosity: 10–30 mPa·s at 25 °C; conductivity > 200 S/cm) were sourced from Sigma–Aldrich. Glycerol (dynamic viscosity: 1412 mPa·s at 25 °C) was obtained from Daejung Chemicals, Korea. COOH-functionalized multiwalled carbon nanotubes (purity: 95 wt.%, electrical conductivity > 100 S/cm) and deionized (DI) water (18.2 MΩ at 24 °C) were also used. All reagents were used, as received.

2.2 | Preparing Humectant-Controlled Hydrogels

Hydrogels were synthesized by combining PVA as the structural matrix, deionized water, and glycerol containing functional additives, including COOH-functionalized carbon nanotubes (COOH-CNTs), LiCl, and PEDOT:PSS, resulting in highly crosslinked networks with exceptional ionic conductivities that were physically compliant for use in strain-sensing applications. Chemical compositions are presented in Tables S1 and S2, while Figure S1 provides a schematic of the step-by-step synthesis process.

2.3 | Characterization

Scanning electron microscopy (SEM, Quattro ESEM, Thermo Scientific) was used to analyze the morphologies of the various hydrogels. The mechanical characteristics of the hydrogels were analyzed using an advanced tensile testing apparatus (MCT-2150, A&D Co.). Water CAs were measured using a goniometer (Phoenix-MT(A), Surface Electro-Optics). The electrical responses of the sensors were evaluated and recorded using a digital source meter (SMU 2611 B, Keithley Instruments, Ltd.). All

26884062, 2026, 9, Downloaded from https://onlinelibrary.wiley.com/doi/10.1002/sstr.70619 by Hanyang University Library, Wiley Online Library on [19/10/2026]. See the Terms and Conditions (https://onlinelibrary.wiley.com/terms-and-conditions) on Wiley Online Library for rules of use; OA articles are governed by the applicable Creative Commons License

sensors were tested at 1 V, with measurements performed under ambient conditions at 25 °C.

2.4 | Preparing Samples for Electro-Mechanical Testing

Specimens for tensile-strength testing were produced by infusing the liquid hydrogel into a 3D-printed mold in accordance with ASTM D638 type-V. A 500 N load cell was used to evaluate the tensile behavior of the hydrogel at a deformation rate of 10 mm/min. We established a complete force–displacement relationship by correlating measured displacements with load data from the pressure cell. The data were subsequently converted into a stress–stretch (s–s) curves. Samples of 50 × 4 × 2 mm in size were prepared for strain sensing. A multipoint strain sensor with multiple copper electrodes was fabricated, with testing conducted under ambient conditions.

3 | Results and Discussion

3.1 | Solvent-Dependent Quasi-Static Tensile Behavior

We selected PVA hydrogels with tunable properties as model systems to test the hypothesis that hydrogel properties are significantly influenced by hydroxyl-containing solvents that are capable of enhancing the mechanical, electrical, and optical performance of the hydrogel while maintaining its stability [39–41]. Uncrosslinked PVA hydrogels were synthesized using three solvents (DI water, EG, and G) and subsequently cured under ambient conditions to facilitate analysis of their solvent–polymer interactions.

The theoretical assumptions for a water-based PVA gel, where a significant number of solvent molecules act as comparatively unbound water, are displayed in Figure 1A; the network is highly hydrated, fragile, and readily broken. The presence of EG or glycerol facilitates the formation of strong H—bonds between the polyol (EG/G), PVA, and water molecules. These interactions increase the bound-solvent fraction, promote the formation of a more densely packed network, and enhance both the stability and bridging effect within the material, consistent with the results reported by Zhou et al. [42] Figure 1B shows that PVA/G (W30/G20 at the bottom) retains its shape well, whereas PVA/water (top) is poorly viscous and highly fluidic. Glycerol, as a hydrophilic triol, decreases the evaporation rate under ambient conditions by forming dense hydrogen-bonding networks with the structural matrix. Here, glycerol serves two functions: it increases the viscosity of the liquid phase, thereby reducing its mobility and also slows the rate at which water moves from the bulk to the surface, thereby preventing rapid surface drying. Hydrogel samples (PVA/G, PVA/EG, and PVA/water, denoted as W30/G20, W30/E20, and W50, respectively) were subsequently

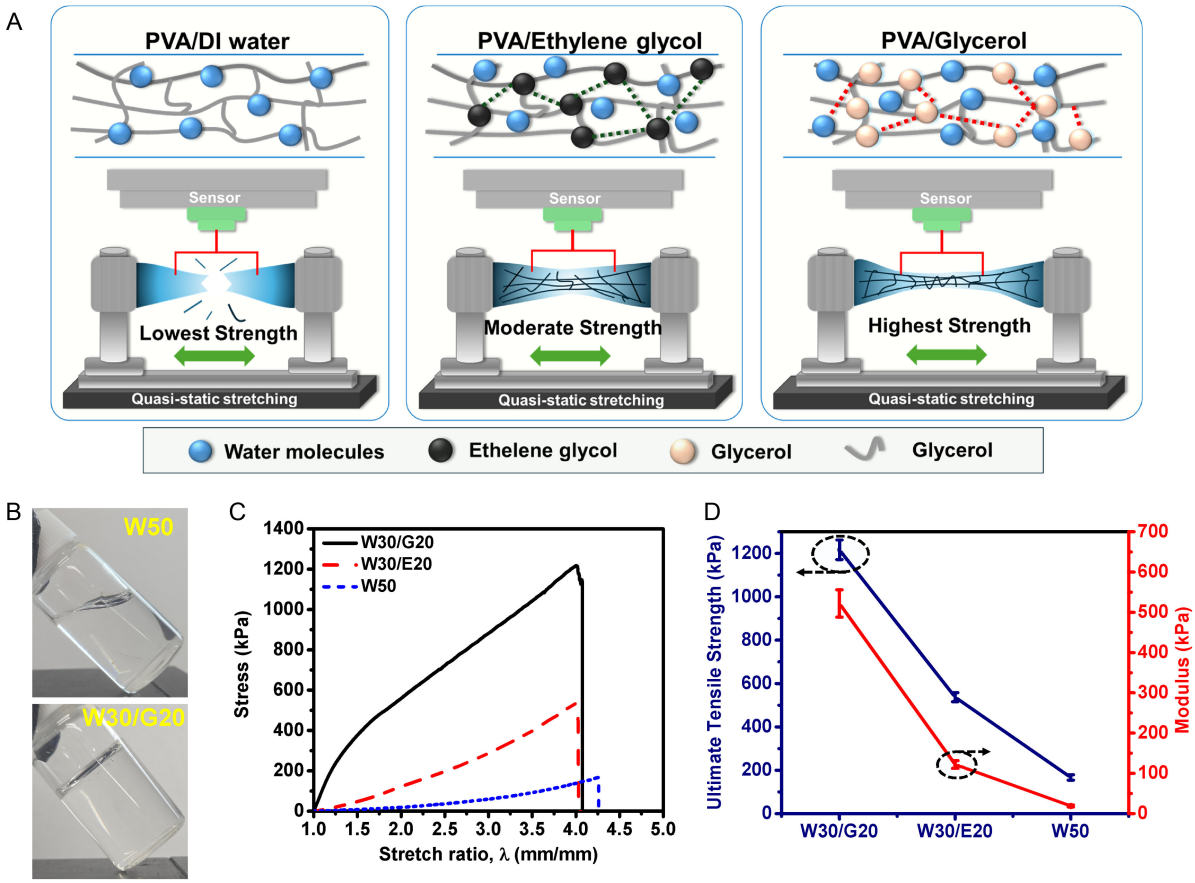

FIGURE 1 | Solvent-dependent mechanical performance of various hydrogels. (A) Schematic depicting PVA-water/EG/G-based solvent systems and their resultant network states. (B) Photographic images showing form-retaining capabilities. (C) Representative stress-stretch curves. (D) Moduli and ultimate tensile strengths for various solvent solutions.

26884062, 2026, 9, Downloaded from https://onlinelibrary.wiley.com/doi/10.1002/sstr.70619 by Hanyang University Library, Wiley Online Library on [19/10/2026]. See the Terms and Conditions (https://onlinelibrary.wiley.com/terms-and-conditions) on Wiley Online Library for rules of use; OA articles are governed by the applicable Creative Commons License

subjected to quasistatic uniaxial tensile testing at a strain rate of 10 mm/min, with resulting s–s curves shown in Figure 1C. The PVA/polyol-based hydrogel exhibited a significantly higher modulus and ultimate tensile strength (UTS) than the other gels: W30/G20 (UTS: 1217 kPa, modulus: 522 kPa) exhibited a superior UTS than W30/E20 (UTS: 537 kPa, modulus: 122 kPa), whose UTS, in turn, was superior to that of PVA/water (UTS: 167 kPa, modulus: 19 kPa) (Figure 1D). These results suggest that incorporating glycerol or ethylene glycol transforms the PVA matrix from a water-diluted fragile physical gel into a denser, more robust, load-bearing structure. In contrast, a hydrogel composed solely of water leads to fewer polymer–polymer interactions and weaker stress transmission, along with lower stiffness and strength and greater variability as a consequence.

3.2 | Chemical Formulation and Hydrogel Surface Chemistry

Considering the outstanding mechanical characteristics of the PVA/G hydrogel, we assessed various water–polyol ratios to systematically adjust hydrogen bonding and plasticization to afford the optimal network density and subsequently correlated the Fourier-transform infrared (FTIR) spectra and CAs with the microstructure. Figure 2A provides a conceptual explanation for how increasing the glycerol concentration while decreasing the water concentration results in more–homogeneous bond strengths with increasing effective polymer concentration, thereby facilitating inter- and intra-crosslinking interactions and greater resistance to dehydration-associated shrinkage. We subsequently incorporated functional additives, including a hygroscopic salt (LiCl) and functionalized carbon nanotubes (COOH-CNTs), which form robust hydrogen bonds that enhance interfacial adhesion and stress transfer, and a conductive polymer (PEDOT:PSS). Conventional hydrogels, which prevalently use freezing and thawing techniques during synthesis owing to their superior crystallinities and crosslinking densities, require long processing times. Moreover, we noticed that our technique afforded a significantly shorter curing time and eliminated the need for prolonged freezing and thawing, as higher glycerol and lower water contents lead to rapid curing (within ~6 h), as shown in Figure 2B. In contrast, lower glycerol and higher water contents resulted in longer curing times. These observations are possibly attributable to the formation of tighter PVA chains that facilitate the formation of a more mature and uniform network, while the cross-linked structure provides stability at a shorter curing time.

Incorporating PEDOT:PSS and COOH-CNTs into the PVA/G hydrogel led to stronger FTIR bands associated with the polymer–filler network (Figure 2C). Stronger C—H stretching contributions are attributable to the PVA/G matrix and the introduced

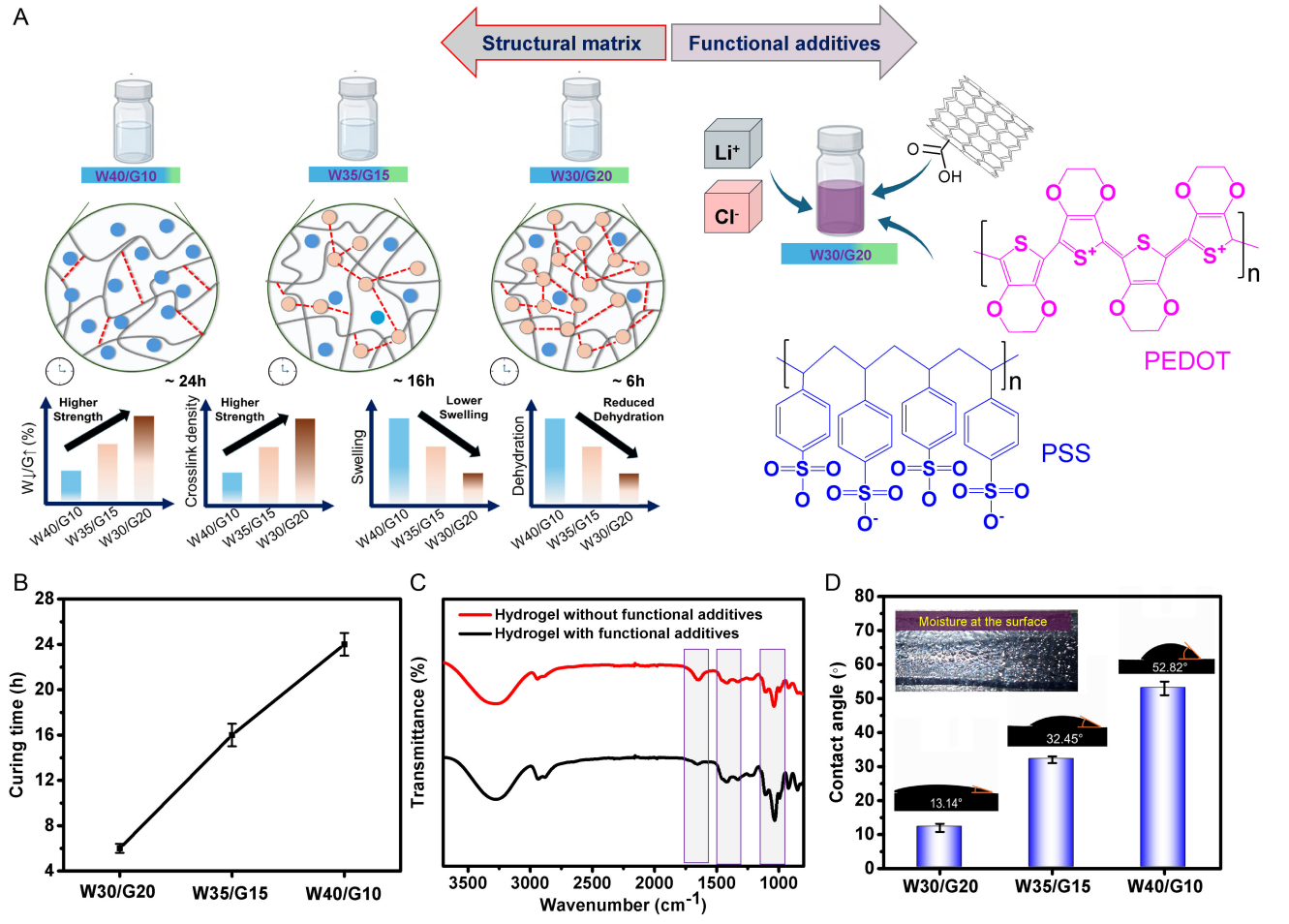

FIGURE 2 | Formulation and physicochemical characterization of water–glycerol polyvinyl alcohol (PVA) hydrogels containing functional additives. (A) Schematic representations of hydrogels prepared with varying water/glycerol ratios and incorporated functional additives. (B) Curing time as a function of hydrogel composition. (C) FTIR spectra and (D) water contact angles that reveal how the formulation affects wettability.

26804062, 2026, 9, Downloaded from https://onlinelibrary.wiley.com/doi/10.1002/sstr.70619 by Hanyang University Library, Wiley Online Library on [19/10/2026]. See the Terms and Conditions (https://onlinelibrary.wiley.com/terms-and-conditions) on Wiley Online Library for rules of use; OA articles are governed by the applicable Creative Commons License

carbonaceous materials, as evidenced by more intense band at around 2900 cm^{-1} [43]. The hydrogel without functional additives exhibits a relatively stronger broad absorption feature near the 1700 cm^{-1} region than the hydrogel containing functional additives. This band is attributed mainly to the bending vibration of absorbed/bound water, with a possible minor contribution from residual carbonyl-containing groups in the base matrix [44, 45]. The stronger bands observed in the ~1400–1450 cm^{-1} range are mostly ascribable to CH_2 bending in base material that possibly overlap with the symmetrical stretching band associated with the reduced carboxylate (COO^-) groups on the COOH-CNTs [46]. A wider ~1200–1000 cm^{-1} band is observed post-doping, indicative of enhanced C—O/C—O—C stretching within the PVA–glycerol hydrogen-bonding system [47], with participation from PSS sulfonate (SO_3^-) and PEDOT-related C—O vibrations, which confirms that PEDOT:PSS had been effectively integrated [48]. Furthermore, the surface wettabilities of the hydrogels were evaluated by measuring contact angles (CAs) to determine how glycerol incorporation impacts key performance parameters relevant to wearable sensing applications. The results reveal that the contact angle decreased from 52.82° to 13.14° with increasing glycerol concentration (and concomitantly decreasing water concentration), with moisture visible on the surface of the material (Figure 2D). The three hydroxyl groups in glycerol are likely to afford a more polar surface capable of forming more hydrogen bonds with water than a surface consisting only of water and PVA. This characteristic increases the polar component of the surface free energy and improves water/surface adhesion. Consequently, the glycerol-rich substance retains and absorbs moisture from the environment, resulting in a lower static water contact angle and a surface on which incoming water droplets are more easily disseminated.

3.3 | Composition-Dependent Strain-Induced Stiffening Behavior

After confirming that the various compounds had been satisfactorily integrated and that the wettability of the surface had changed in an appropriate manner, we next validated mechanical properties, specifically rigidity and elasticity, under uniaxial quasi-static loading conditions at different water (40/35/30 g) and glycerol (10/15/20 g) loadings. Quasi-static s–s curves are displayed in Figure 3A, from which a detailed discussion of the maximum load-bearing capability, defined by the modulus and stretch ratio, is presented. Incrementally incorporating glycerol (from W40/G10 to W30/G20) led to a systematic increase in the functional cross-linking density, which strengthened the PVA hydrogel as a consequence; this modification resulted in a 39% increase in UTS and a 111% increase in the modulus. Conversely, the stretch ratio exhibited an inverse relationship: a denser network restricts chain slippage, thereby limiting the maximum achievable stretch ratio (Figure 3B). The shifts in the C—O band observed in the FTIR spectra suggest that increasing the glycerol concentration leads to a more uniform and dense microstructure characterized by fewer defects and less phase separation. Additionally, it facilitates a more homogeneous dispersion and enhances hydrogen bonding between the PVA and glycerol throughout the material. The smooth SEM cross-sectional fracture faces shown in Figure 3C1 and C2 provide direct morphological evidence in support of these mechanical observations. Cyclic s–s data acquired with increasing maximum stretching ratio (1.25–3.5) highlights energy-dissipating capability of the hydrogel (Figure 3D). We also analyzed the tensile behavior of the hydrogel with or without functional additives, and detailed discussions are provided in the Supporting Information (Figure S2A–C). The loading–unloading curves show hysteresis loops that progressively become larger with increasing maximum stretch, which reveals the presence of active strain-activated energy-dissipating processes that help to protect the network from fracturing. This hysteresis behavior is considerably stretching-dependent: the hysteresis loop area is very small at low stretch ($\lambda < 1.5$), with hysteresis loops that practically coincide during cycling and only slight stress drops observed, highlighting the exceptional anti-fatigue characteristics of the hydrogel. On the other hand, subsequent cycles exhibited little variation at high stretch ratios ($\lambda > 1.5$) following energy dissipation in the initial cycle, with only a modest reduction in stress recorded during continued cycling.

Moreover, we further analyzed strain softening and modulus reduction across the first two loading–unloading cycles to assess the primary responses at four hydrogel strain (strain = stretch ratio-1) levels (15%, 35%, 70%, and 105%) as the most significant change was observed between the first and second cycles. In contrast, nearly identical results were observed in subsequent cycles (Figure S3A). These findings reveal very little softening at 15% strain, along with a minor decrease in peak stress and a modulus reduction of less than 10%, suggestive of mostly reversible displacement characterized by brief physical contacts that break and quickly reform (Figure S3B—D). Conversely, softening escalates significantly at ≥70% strain, as does the reduction in modulus (surpassing 50% at 105% strain), consistent with notable Mullins-type softening induced by irreversible network reconfiguration (e.g., chain slippage/alignment and partial disentanglement) and the disruption of weaker sacrificial interactions when substantially deformed [49]. This strain-dependent shift reveals that while the network maintains its mechanical stability under low physiologically realistic cyclic stresses, higher strains lead to accumulated damage and a permanent reduction in hydrogel stiffness.

Figure 3E–G displays the hysteresis behavior of three distinct hydrogel combinations at a constant stretch ratio (λ) of 2.7, which reveals that W30/G20 exhibited the lowest hysteresis ratio of ~25.2%, indicative of enhanced elastic energy storage and superior recovery despite its higher modulus (Figure 3H). Conversely, W35/G15 and W40/G10 exhibited significantly larger hysteresis ratios of approximately 55% and 50%, respectively, indicative of optimal energy dissipation, with the dissipated energy accounting for nearly half of the work performed by the external force. The hysteresis ratio, as the ratio of the enclosed loop area to the total loading energy, quantifies energy dissipation. Further, dynamic mechanical analysis investigated the small-amplitude viscoelastic behavior of the optimized hydrogel sample W30/G20 across 2–10 Hz (Figure S4). The storage modulus (E') consistently exceeded the loss modulus (E") throughout the frequency spectrum, although the ratio remained significantly below one, indicating predominantly elastic, solid-like behavior. The storage modulus increased from approximately 120–160 kPa but remained relatively low overall, with the ratio progressively declining to about 0.06 at higher frequencies. This frequency-dependent rigidity indicates that during brief

26884062, 2026, 9, Downloaded from https://onlinelibrary.wiley.com/doi/10.1002/sstr.70619 by Hanyang University Library, Wiley Online Library on [19/10/2026]. See the Terms and Conditions (https://onlinelibrary.wiley.com/terms-and-conditions) on Wiley Online Library for rules of use; OA articles are governed by the applicable Creative Commons License

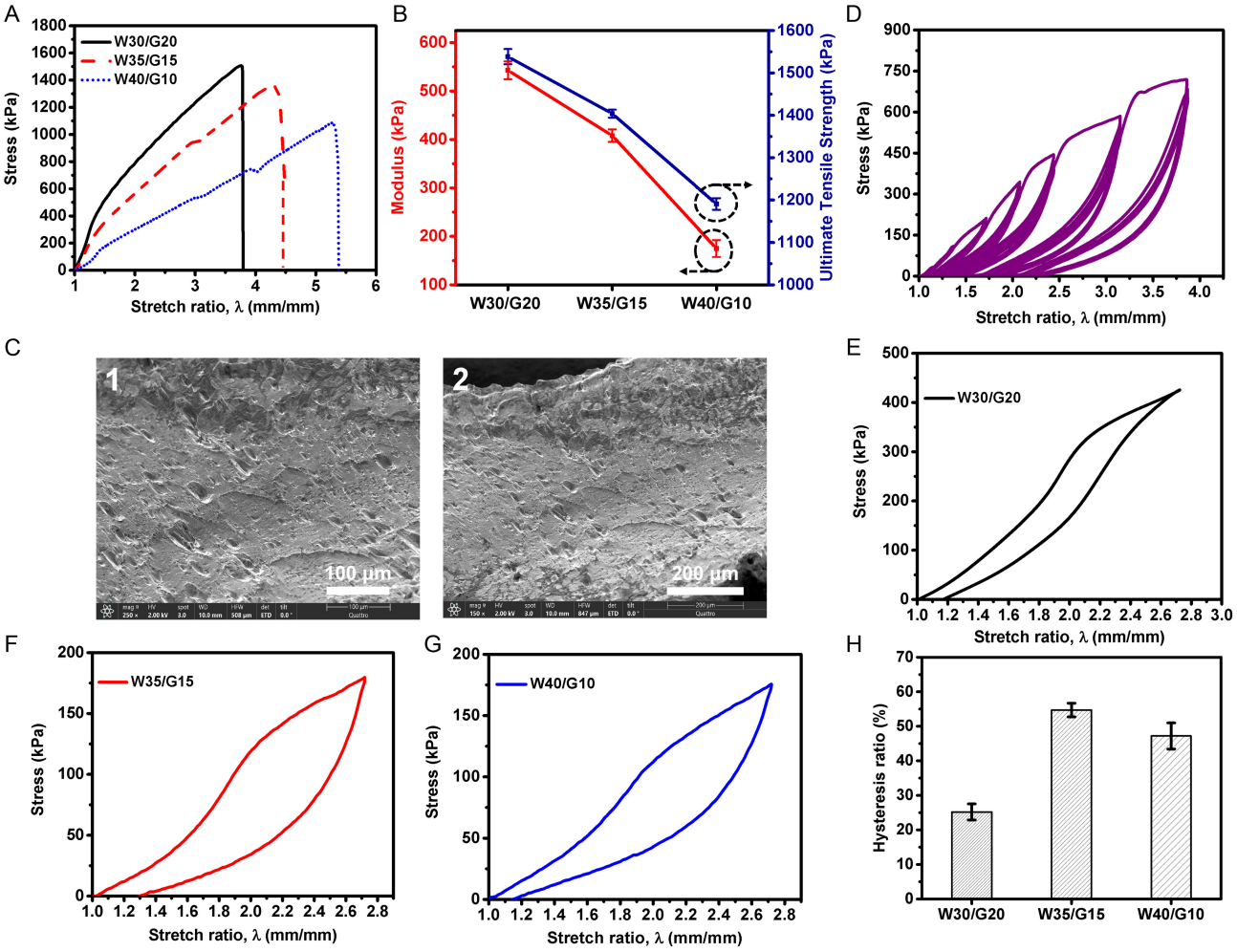

FIGURE 3 | Quasi-static stress–stretch characteristics of various hydrogels. (A) Stress–stretch (s–s) curves for various hydrogel compositions (W30/G20, W35/G15, W40/G10), and (B) moduli and ultimate tensile strengths for these samples. (C) Cross-sectional SEM images of the W30/G20 sample. (D) Cyclic stress–stretch curves acquired at different stretch rates, and (E–G) cyclic response data for the W30/G20, W35/G15, and W40/G10 specimens. (H) Hysteresis ratio according to material composition.

deformation intervals, the PVA chains and reversible supramolecular interactions do not have enough time to reconfigure significantly, resulting in a greater proportion of mechanically stored energy. Similar elastic-dominant characteristics have been reported for PVA-based hydrogels and hydrogen-bonded PVA/glycerol networks, where physical interactions and chain entanglement maintain network stability during dynamic deformation.

3.4 | Hydration-Driven Mechanical and Morphological Behavior

Hydrogels are composed of interchain networks and randomly arranged water molecules, the key characteristics of which are their abilities to swell and dehydrate. The behavior of a hydrogel is significantly influenced by the size of its surface pores, the intermolecular spaces within its network, and its hydrophilic and hydrophobic properties. For instance, a hydrogel with a high cross-linking density exhibits little swelling, whereas one with large pores may grow considerably and absorb more than its own weight in water [50]. The dependability of a hydrogel is closely correlated with its swelling and dehydration properties that reveal whether its structure, mechanical properties, and interfaces are preserved over time or undergo stress-induced rearrangements that may be functionally advantageous or lead to failure.

Figure 4A displays a schematic of the swelling and shrinking behavior observed in the three distinct types of hydrogel over 1 week. The samples were first swollen by immersion in DI water and then dehydrated by exposure to ambient conditions. Images of the hydrogel samples before and after swelling and dehydration are shown in Figure S5. Sample weights were measured hourly to assess swelling and every 12 h to evaluate dehydration. W30/G20 was found to exhibit lower variabilities in both the swelling ratio (~25%) and dehydration (~−10%) than W35/G15 and W40/G10. In contrast, W35/G15 and W40/G10 exhibited equilibrium swelling and dehydration ratios of about 50% and −40% and 90% and −75%, respectively, as shown in Figure 4B,C. The SEM image of W30/G20 (Figure 4D) shows morphological changes near the outermost edges of the dehydrated samples, that indicate the most vulnerable areas. The edges appear degraded or fractured (Figure 4D1 and D2) because the dried structure cannot accommodate stresses plastically; as a result, the fracture surface displays genuine cracking, with dehydration-induced stresses leading to microcracks and edge chipping. Conversely, Figure 4D3

26884062, 2026, 9, Downloaded from https://onlinelibrary.wiley.com/doi/10.1002/sstr.70619 by Hanyang University Library, Wiley Online Library on [19/10/2026]. See the Terms and Conditions (https://onlinelibrary.wiley.com/terms-and-conditions) on Wiley Online Library for rules of use; OA articles are governed by the applicable Creative Commons License

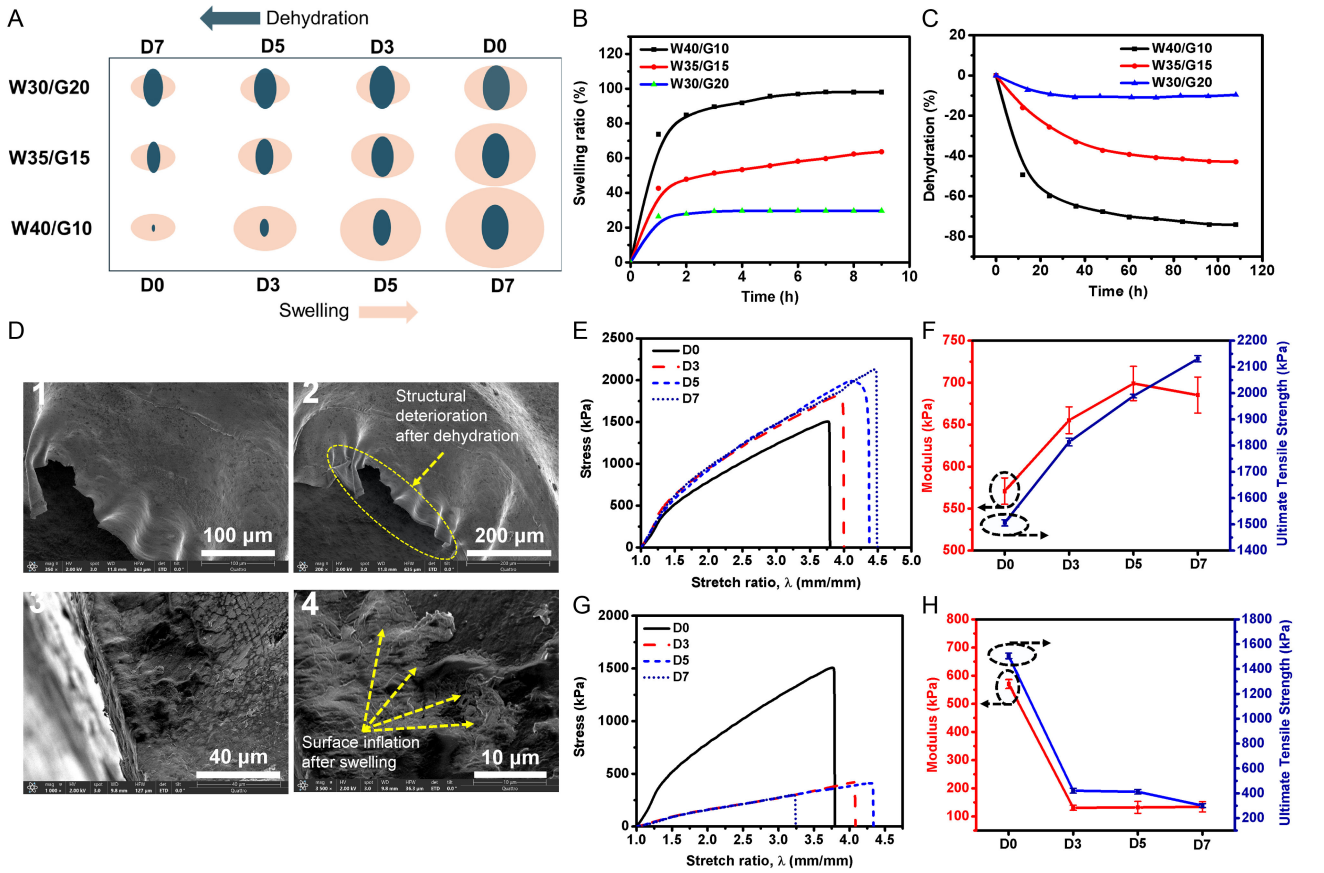

FIGURE 4 | Mechanical and morphological behavior of hydrogels influenced by hydration. (A) Depicting swelling and dehydration. (B) Swelling kinetics (swelling ratio vs. time). (C) Dehydration kinetics (dehydration ratio vs. time). SEM images of (D1–2) dehydrated and (D3–4) swollen hydrogels. (E) Representative s–s curves after dehydration from day 0 to day 7, (F) corresponding moduli and UTS values, (G) s–s curves of swollen hydrogels, and (H) corresponding moduli and UTS values.

and D4 show that the swelling network deforms during hydration owing to fewer surface constraints, leading to outward expansion and a locally convex, inflated appearance rather than a flawless flat surface.

We conducted a comprehensive investigation with the aim of understanding the changes in mechanical characteristics observed for both swollen and dehydrated samples when subjected to uniaxial loading under quasi-static conditions. To that end, we used as-prepared dogbone-shaped samples that were immersed in DI water to assess swelling and exposed to ambient conditions to evaluate dehydration. Experiments on the W30/G20 sample were performed at 2-day intervals over a 7-day duration, with the key experimental observations presented in Figure 4E–H. The intensity of the s–s curve was observed to increase gradually as surplus water was removed from the structure during dehydration (Figure 4E), which increased the polymer concentration and led to more polymer-chain entanglement and a higher effective crosslinking density, with both the UTS and modulus increasing by ~41% from Day 0 (D0) to Day 7 (D7) (Figure 4F). Relative extension was observed to increase despite the increasing dryness, which is ascribable to the presence of hygroscopic substances that preserve the plasticity of the network and inhibit brittleness. Chain movement was not entirely immobilized, which enabled the more densely interconnected network to undergo significant elongation before breakdown. Conversely, the s–s curves of the swollen samples reveal a substantial decline in performance between D0 and D3, with an ~72% lower modulus and a ~77.2% lower UTS recorded. Notably, no significant change in modulus or UTS was observed beyond D3 (Figure 4H). Swollen gels often have larger pores that facilitate viscous flow and fracture propagation at lower stress levels, along with a lower tensile strength as a consequence. Additionally, polymeric density relaxation following swelling led to less stiffness compared to that observed for the denser, partly dehydrated condition.

3.5 | Fracture Mechanics and Toughness Characterization

Based on the remarkable dimensional stability observed for the hydrogels during the dehydration and swelling experiments, we further examined their fracture behavior in pure shear experiments. We assessed the fracture toughness of three hydrogel samples (W30/G20, W35/G15, and W40/G10), each 50 × 10 × 2 mm in size. Figure 5A shows a schematic of the tested uncut and precut samples, with further samples shown in Figure S6A–C. Movie S1 is a video of the pure shear test used to examine the fracture behavior of a sample. Figure 5B displays images of a 20 mm precut hydrogel sample used during testing, which shows that while the crack widens gradually with increasing elongation, its length nevertheless remains almost constant even at a stretch ratio of 1.7.

26884062, 2026, 9, Downloaded from https://onlinelibrary.wiley.com/doi/10.1002/sstr.70619 by Hanyang University Library, Wiley Online Library on [19/10/2026]. See the Terms and Conditions (https://onlinelibrary.wiley.com/terms-and-conditions) on Wiley Online Library for rules of use; OA articles are governed by the applicable Creative Commons License

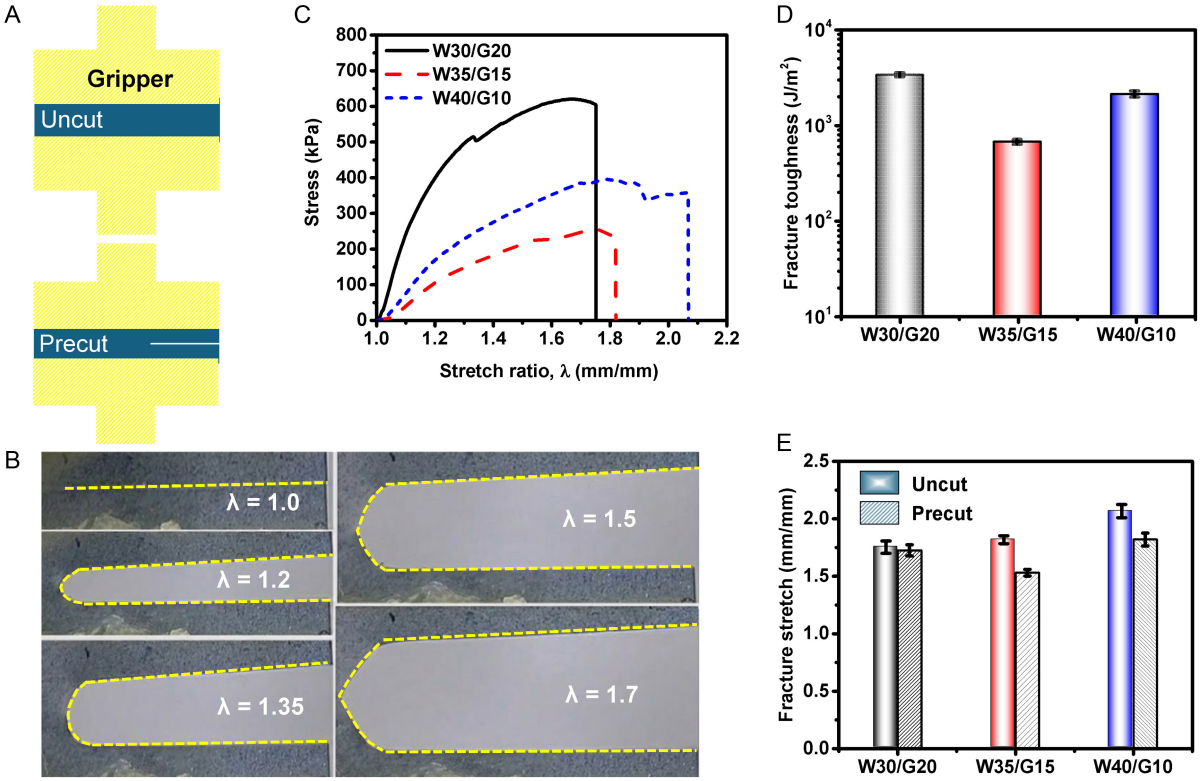

FIGURE 5 | Fracture behavior of hydrogels with different compositions. (A) Schematics of uncut and precut samples used in the experiments. (B) Snapshots of a W30/G20 hydrogel sample at various deformations. (C) Representative s–s curves for hydrogels with different compositions (W30/G20, W35/G15, and W40/G10). (D) Fracture toughness measured during pure shear testing. (E) Fracture stretches for uncut (plain bars) and precut (patterned bars) samples with different compositions (W30/G20, W35/G15, and W40/G10).

Figure 5C reveals that W30/G20 exhibited a superior modulus of ~621 kPa, which is 2.4 times that of W35/G15 (~255 kPa) and 1.6 times that of W40/G10 (~396 kPa). Interestingly, W40/G10 exhibited a higher fracture strength than W35/G15 despite its higher water content, which is an unusual fracture-strength observation. This trend is ascribable to the slightly higher initial water content and low glycerol fraction in W40/G10, which led to substantial dehydration during room temperature (RT) curing prior to complete network fixation. This premature dehydration increases the effective crosslinking density through volumetric contraction despite the constant number of chemical crosslinks (Equation (1)). This affine network prediction is consistent with the observation that the modulus scales with the effective density of the elastically active chains according to

$$E \approx 3\nu k_B T \tag{1}$$

where ν is the effective crosslinking density per unit volume, k_B is the Boltzmann constant, and T is the absolute temperature.

For further clarification, we also compared the fracture s–s behavior of samples cured at RT and under freeze–thaw conditions, with the results presented in Figure S7 revealing similar patterns: W30/G20 exhibited a fracture toughness of approximately 3.37×10^3 J/m^2, indicative of superior crack resistance compared to those of the other two compositions (W35/G15: 6.6×10^2 J/m^2 and W40/G10: 2.1×10^3 J/m^2) (Figure 5D). These findings are in qualitative agreement with the Lake–Thomas framework, which indicates that a higher network density enhances the intrinsic fracture energy [51]. Nevertheless, the observed compositional dependence suggests that toughness is also influenced by the dynamic dissipation processes (reversible O—H and chain mobility), which are not addressed by the standard Lake–Thomas framework established for permanently crosslinked elastomers.

The W30/G20 sample exhibited a fracture stretch of approximately 1.75 in its uncut condition and 1.73 in its precut condition (Figure 5E), which is essentially identical performance. This observation is consistent with a notch-insensitive response in which deformation is equally distributed across the network, regardless of the presence of cracks. Conversely, the W35/G15 composition exhibited a fracture stretch of approximately 1.82 in its uncut condition but a dramatically lower value of 1.53 in its precut condition, indicative of brittle, crack-prone behavior. The W40/G10 composition exhibited the greatest fracture stretch (~2.07) under uncut conditions; however, the significantly lower value recorded under precut conditions is indicative of partial notch sensitivity. The superior fracture toughness and fatigue resistance of the W30/G20 hydrogel result from the equilibrium between network fortification and molecular reversibility. While large energy dissipation can significantly improve hydrogel fracture toughness, it does not necessarily lead to a proportional increase in the fatigue threshold [52]. Moreover, the molecular structure of the load-bearing polymer network, especially polymer chain entanglement, strongly influences fracture and fatigue resistance under cyclic loading [37]. In the current framework,

26884062, 2026, 9, Downloaded from https://onlinelibrary.wiley.com/doi/10.1002/sstr.70619 by Hanyang University Library, Wiley Online Library on [19/10/2026]. See the Terms and Conditions (https://onlinelibrary.wiley.com/terms-and-conditions) on Wiley Online Library for rules of use; OA articles are governed by the applicable Creative Commons License

the glycerol-abundant microenvironment fosters significant hydrogen bonding between PVA, glycerol, and water, thus enhancing the effective network density and mitigating rapid dehydration. At the same time, sufficient chain mobility is preserved, enabling molecular reconfiguration and stress redistribution during deformation. Collectively, these results indicate that the advantageous fracture and fatigue characteristics stem from the synergistic influence of network densification, reversible molecular interactions, preserved chain mobility, and functional additive enhancement, rather than solely from conductive-filler inclusion.

3.6 | Hydrogel Fatigue Behavior

Fatigue resistance was evaluated through cyclic crack growth experiments using a pure-shear sample with a preexisting crack. Specimens were subjected to repeated loading at various maximum stretch ratios (λ_x), with the results recorded as functions of cycle number, as shown in Figure 6A. Cyclic loading experiments were also performed on uncut specimens under the same maximum stretch conditions to measure the energy release rate, G, (Figure 6B). Stress softening caused by network rearrangement during initial cycling prompted us to use the stable s–s profiles for the100th cycle to calculate strain energy densities and energy release rates. Figure 6C reveals that maximum stress decreases progressively during initial cycling but stabilized after the 20th cycle, indicative of reversible chain entanglement that is consistently reorganized. The stabilized hysteresis loops shown in Figure 6D demonstrate fully reversible dissociation/reformation of glycerol-mediated H-bond networks and chain entanglements under cyclic dehydration conditions, which highlights its excellent fatigue resistance for use in long-term strain-sensing applications.

Fatigue testing also revealed that crack growth depends strongly on applied G, which is given by Equation (2) for a pure shear geometry

$$G = W(\lambda_x)H \tag{2}$$

where $W(\lambda_x)$ is the strain energy density at λ_x and H is the very initial height of the specimen. Strain energy density is derived from the consolidated stress curve (100th cycle) according to

$$W(\lambda_m) = \int_1^{\lambda_x} \sigma(\lambda)\, d\lambda \tag{3}$$

where $\sigma(\lambda)$ is the nominal stress. We selected the 100th cycle to minimize the influence of stress softening observed during the initial loading cycles (see Equation (3)).

Figure 6E shows relationships between crack extension and cycle number at two values of G: 114.88 J/m^2, which led to stable/negligible crack growth (~0.32 mm crack extension after each 500 cycle till 3000 cycles; later, it becomes stable with no crack extension) that indicates the applied driving force is below the intrinsic fatigue threshold. On the other hand, accelerated crack growth (active propagation) was observed from the early cycles onward at G=409.62 J/m^2, which indicates that this value of G significantly exceeds the fatigue threshold. The crack development rate

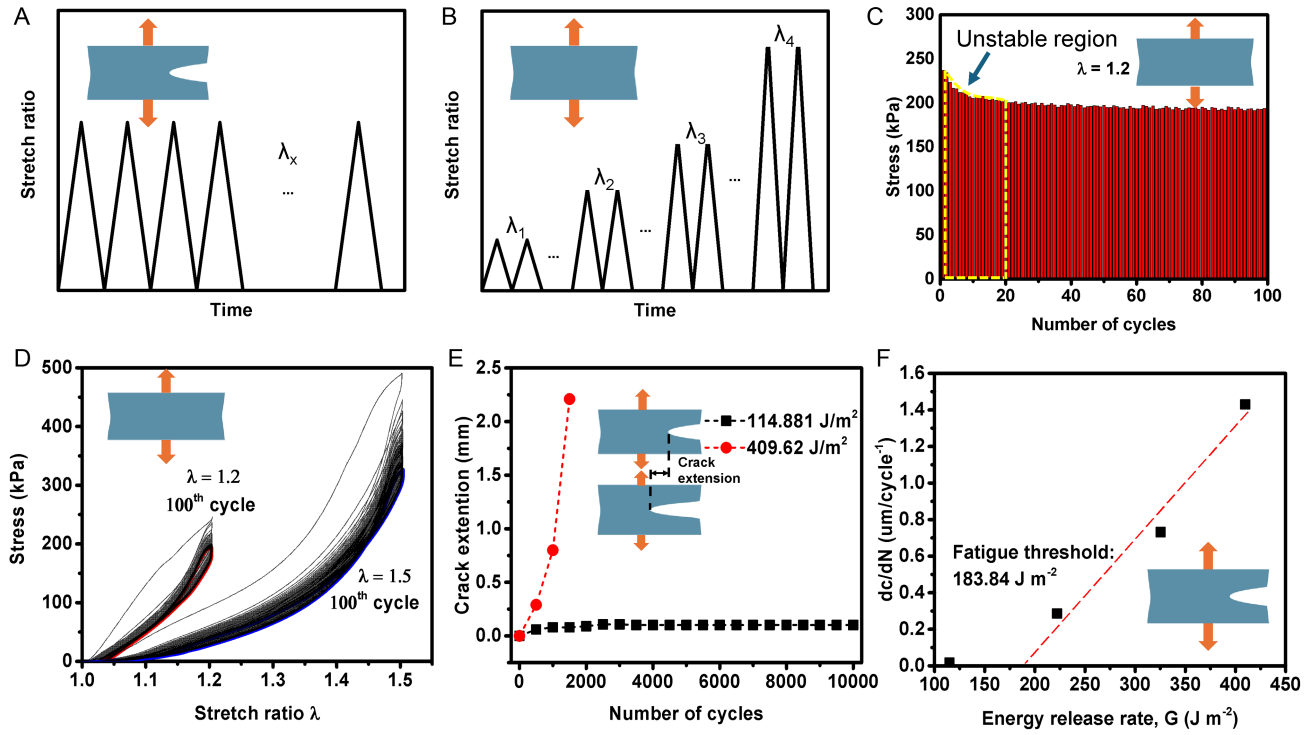

FIGURE 6 | Fatigue-resistance behavior of the W30/G20 hydrogel. Crack extensions in (A) precut and (B) uncut samples loaded to maximum stretch ratio λ_x. (C) The maximal stress of each cycle decreased to a stable value at λ=1.2. (D) Stable hysteresis loops observed after 100 cycles at λ=1.2. (E) Crack growth in precut samples with energy release rates of 114.88 and 409.62 J/m^2. (F) Relationship between crack extension (dc/dN) and energy release rate.

26884062, 2026, 9, Downloaded from https://onlinelibrary.wiley.com/doi/10.1002/sstr.70619 by Hanyang University Library, Wiley Online Library on [19/10/2026]. See the Terms and Conditions (https://onlinelibrary.wiley.com/terms-and-conditions) on Wiley Online Library for rules of use; OA articles are governed by the applicable Creative Commons License

(dc/dN) in the stable crack-growth phase was determined from the gradient of the relationship between crack length and cycle number (Equation (4))

$$\frac{dc}{dN} = A(G - \Gamma_0) \tag{4}$$

where A is a fitting constant and Γ_0 is the fatigue threshold, which revealed that dc/dN and G are linearly correlated throughout the examined range (Figure 6F). The determined Γ_0 value reveals that the optimal glycerol–water combination fosters the formation of a dense, highly linked hydrogen-bonding network in which glycerol acts as a multifunctional bridge plasticizer [53, 54]. Reversible interactions between PVA, glycerol, and water reinforce interchain interactions while facilitating dynamic bond exchange, thereby establishing a robust chemical foundation for superior energy dissipation and resilience to fatigue damage [55, 56]. The comprehensive mechanical characteristics derived from the aforementioned tests are presented in Table S3. To further benchmark the mechanical performance of the present hydrogel, Tables S4 and S5 provide quantitative comparisons with recently reported mechanically durable and environmentally stable hydrogel systems. The present PVA/glycerol hybrid hydrogel demonstrates a favorable combination of tensile strength, fracture toughness, fatigue resistance, dehydration stability, and electromechanical sensing performance, underscoring its potential for mechanically robust and environmentally durable wearable sensing applications.

3.7 | Electro-Mechanical Sensing Performance

Incorporating functional ingredients in a hydrogel can endow it with hybrid ionic–electronic conductivity. LiCl is hygroscopic, readily absorbs atmospheric moisture, and is fully soluble in water or glycerol to afford tiny, exceptionally mobile Li^+ and Cl^- ions [57]. These ions constitute the primary ionic conduction channels inside a hydrogel and are responsible for the variations in resistance or capacitance observed during deformation. Conversely, PEDOT serves as a π-conjugated electrical conductor, while PSS bears hydrophilic sulfonate groups capable of forming hydrogen bonds or engaging in electrostatic interactions with PVA chains and Li^+ [58].

Strain sensitivity was assessed by measuring relative changes in electrical resistance ($\Delta R/R_0$) for the W30/G20 hydrogel under various stretching conditions. Figure 7A reveals that resistance variations during uniaxial stretching are ascribable to changes in the ionic route length (L) and cross-sectional area (a) (L/a). Each hydrogel segment has identical cross-sectional dimensions and stiffness when geometrically uniform along its length; consequently, local strain (ε_x) is equivalent to the global strain (ε_g) (Equation (5))

$$\varepsilon_x = \varepsilon_{neck} = \varepsilon_g \tag{5}$$

Therefore, the sensor obeys the relationship:

$$\frac{R}{R_0} = (1 + \varepsilon_g)^2 \tag{6}$$

Nevertheless, the cross-sectional area of a hydrogel decreases significantly as it is stretched according to Equation (6); consequently, the local strain exceeds the global strain (Equation (7))

$$\varepsilon_x = \varepsilon_{neck} = k_x \varepsilon_g \tag{7}$$

where k_x is the strain concentration factor. The neck, with its narrowest cross-section and most effective current path, largely determines the overall resistance in the distorted state. The total change in resistance during stretching is given by Equation (8)

$$\frac{R}{R_0} = (1 + k_x \varepsilon_g)^2 \tag{8}$$

Accordingly, even small macroscopic deformations result in significant relative shifts in resistance owing to the ability of the deformation-dependent sensor design to amplify strain in the ion-channel-percolated network of the neck region.

The gauge factor (GF), defined as $(\Delta R/R_0)/\varepsilon$, was used to assess the sensor's strain sensitivity. Where, $\Delta R = R - R_0$, R_0, and R define initial resistance and resistance under strain, respectively. Moreover, the resistance–strain relationship was analyzed using segmented linear fitting because different linear responses were observed across the full strain range. Specifically, fitting was performed in Origin over three strain intervals: 0%–100%, 100%–200%, and 200%–300%, and the slope of each fitted segment was defined as the GF for that interval. The sensor exhibited a $\Delta R/R_0$ value that increases with increasing strain attenuation, as shown in Figure 7B, where GF values of 1.43, 1.66, and 1.46 correspond to strains of 0%–100%, 100%–200%, and 200%–300%, respectively, with the GF exhibiting an unusual behavior at strains greater than 200%. This trend is consistent with the emergence of a secondary source of conductivity that is potentially ascribable to PEDOT:PSS and the development of microcracks and network rearrangement.

Table S6 compares GF and practical strain ranges from several recent research articles that demonstrate sufficient sensitivity. Also, Table S7 presents a comparison of the mechanical and electromechanical properties of the PVA-based hydrogel. Moreover, Figure 7C reveals reaction and recovery times of 300 and 207 ms, respectively; this fast reaction time is suitable for real-time monitoring in highly sensitive sensor applications.

The hydrogel sensor was strained in the 0%–50% range and then reverted to zero strain (Figure 7D). The response of the sensor progressively increased as the applied strain was incrementally varied from 0% to 15%, and then to 25%, 50%, 25%, 15%, and 0%, owing to polymeric chain stretching and ion migration. The resistance reverted to its original value when the strain was recovered, which is attributable to the exceptional elasticity and resilience of the hydrogel substrate and highlights the remarkable stability of the sensor during multicycle testing. Moreover, the sensor demonstrated very steady resistance responses during loading and unloading, which are crucial attributes of a high-fidelity sensor. Taken together, the results presented above reveal that the hydrogel sensor performs well at both low and high strains. Moreover, the recorded signals exhibited waveforms with identical amplitudes but distinct frequencies when stretched at 20, 100, 200, and 300 mm/min at a constant strain of 25% (Figure 7E), consistent with theoretical predictions. The hydrogel

26884062, 2026, 9, Downloaded from https://onlinelibrary.wiley.com/doi/10.1002/sstr.70619 by Hanyang University Library, Wiley Online Library on [19/10/2026]. See the Terms and Conditions (https://onlinelibrary.wiley.com/terms-and-conditions) on Wiley Online Library for rules of use; OA articles are governed by the applicable Creative Commons License

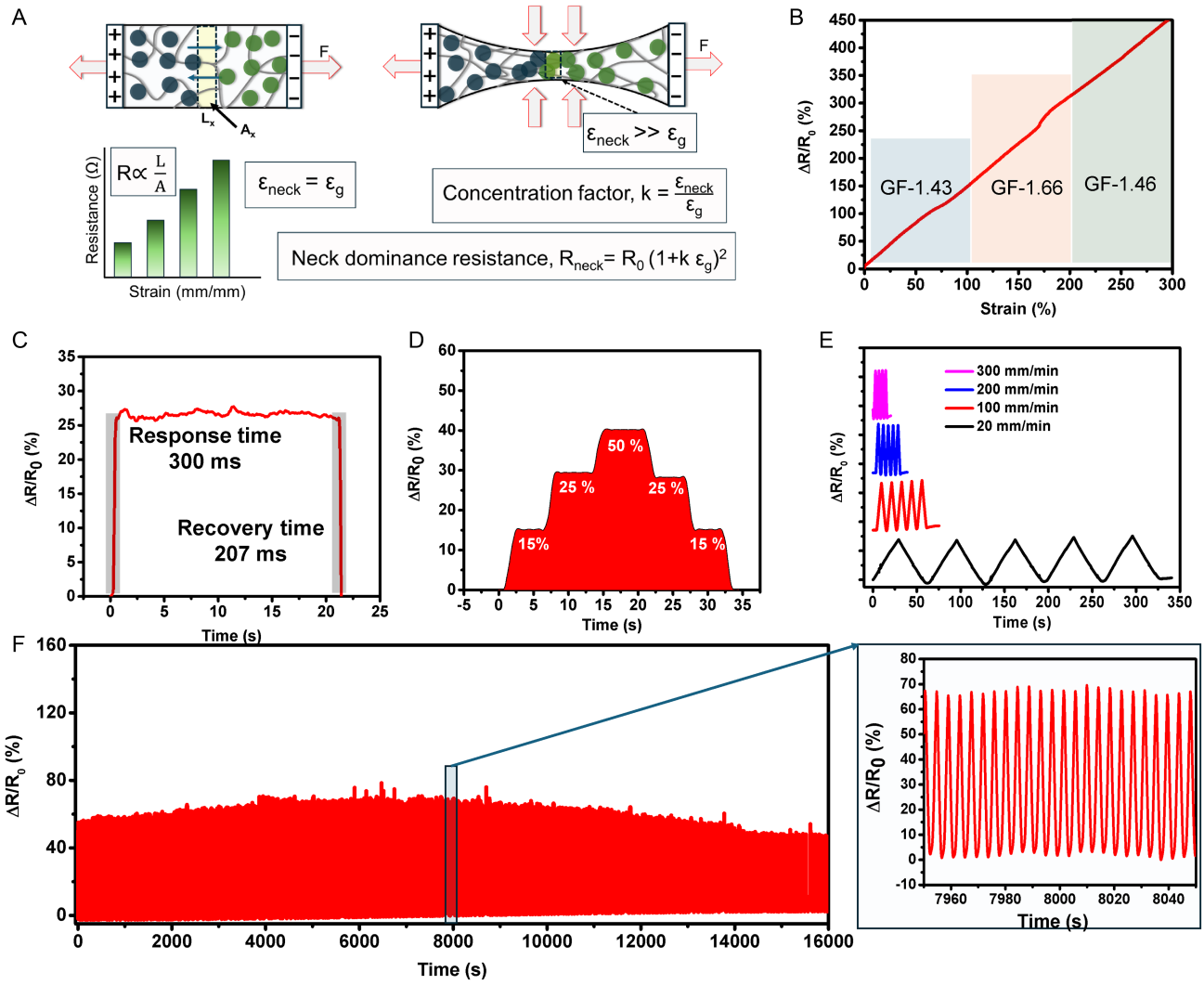

FIGURE 7 | Electro-mechanical sensing properties of the W30/G20 hydrogel. (A) Schematic depicting strain concentration and neck-dominated resistance under uniaxial stretching conditions. (B) Gauge factors in various strain ranges (0%–100%, 100%–200%, and 200%–300%). (C) Response and recovery times during stretching and releasing. (D) Stepwise $\Delta R/R_0$ responses of the hydrogel in response to a random sequence strain loading. (E) Uniform responses at 25% strain and various frequencies. (F) Cyclic stability testing over 5000 stretching/releasing cycles at 35% strain.

sensor exhibited stable variations in relative resistance, indicative of the absence of a frequency dependence. This capacity to sustain a consistent signal during constant deformation reveals considerable signal reliability for assessing static strain. The repeatability and endurance of the hydrogel sensor were assessed through cyclic loading–unloading experiments with the aim of observing durable deformation-dependent sensing at fixed strain (35%, 300 mm/min), the results of which are shown in Figure 7F. $\Delta R/R_0$ responded steadily across 5000 longitudinal s–s cycles, with very little drift observed at the end. A long-term stability test was performed by comparing the as-prepared hydrogel with a sample stored for 3 months. The experimental results are presented in the Supporting Information (Figure S8). Moreover, we evaluated the sensor's reliability under perspiration-relevant conditions by subjecting it to 100 cyclic stretching cycles at 25% strain in both dry and artificial sweat environments. Artificial perspiration, consisting of NaCl, urea, and lactic acid (pH approximately 6.5), was applied to the sensor during cyclic deformation. The sweat-exposed sensor showed a consistent $\Delta R/R_0$ response with minimal baseline drift. In contrast, under dry conditions, the sensor showed a slight, gradual baseline shift during cycling. These results indicate that exposure to a sweat-like ionic environment does not compromise electromechanical stability, supporting the hydrogel sensor's suitability for wearable skin monitoring. Further, to elucidate the origin of the enhanced electrical performance, the conductivity of the hybrid hydrogel was compared with that of hydrogels containing only LiCl or only PEDOT:PSS. The results, as shown in Figure S10, demonstrate that the hybrid structure achieves higher conductivity than either ionic or electronic conduction alone. These findings indicate that the hydrogel remains robust after storage and that the hybrid conductive network contributes to sustained, enhanced sensing performance over time.

3.8 | A Flexible Multi-Channel Forearm Muscle Sensor

We developed a hydrogel sensor endowed with exceptional conductivity, stretchability, and water-retaining capabilities, thereby addressing the trade-off between conductivity and flexibility. Hybrid LiCl/PEDOT:PSS conduction ensures stable contact

26884062, 2026, 9, Downloaded from https://onlinelibrary.wiley.com/doi/10.1002/sstr.70619 by Hanyang University Library, Wiley Online Library on [19/10/2026]. See the Terms and Conditions (https://onlinelibrary.wiley.com/terms-and-conditions) on Wiley Online Library for rules of use; OA articles are governed by the applicable Creative Commons License

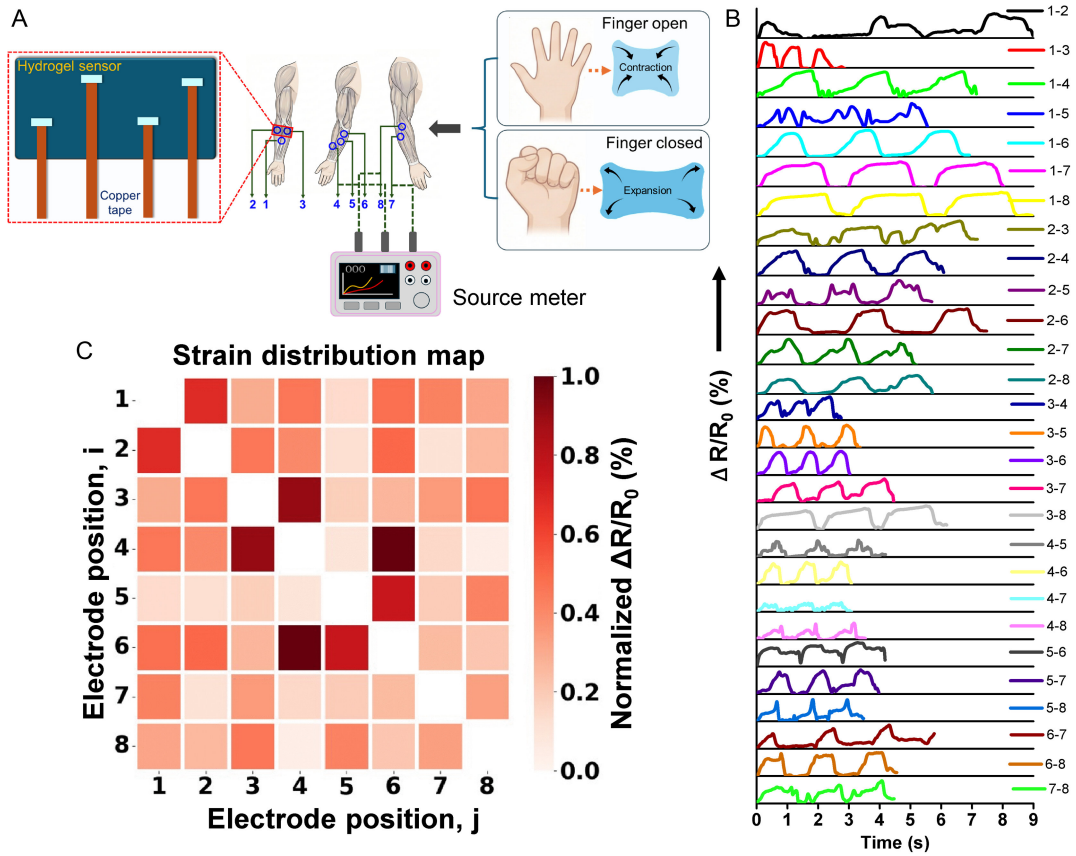

FIGURE 8 | A flexible hydrogel sensor for monitoring forearm muscle activity. (A) Schematic showing the multi-channel detection of forearm muscle contraction and relaxation using a hydrogel sensor array. (B) $\Delta R/R_0$ signals recorded from various electrode pairs of an eight-channel hydrogel sensor. (C) Heatmap of spatial strain distribution across electrode pairs based on normalized $\Delta R/R_0$ responses.

resistance under repetitive deformation. Figure 8A shows a hydrogel sensor pad with integrated copper-tape electrodes affixed with silver paste that create a flexible interface for radial–ulnar muscle-strain monitoring. Electrodes 1–8 were positioned along the dorsal forearm, including the superficial extensor muscle group (e.g., extensor carpi radialis longus and brevis, extensor digitorum, and extensor carpi ulnaris).

Deformation produces anisotropic strain within the ionically sensitive hydrogel matrix, which affects interelectrode route lengths, cross-sectional regions, and ion mobility efficiency, resulting in observable variations in electrical resistance between distinct electrode pairs. The $\Delta R/R_0$ value for each channel was calculated by selecting two representative electrodes (1–8) and measuring changes in resistance during muscle expansion and contraction after the hydrogel pad was fixed to the forearm (Figre S11). These signals arise from deformation-induced changes in resistance associated with muscle motion rather than from direct electrophysiological signal acquisition. In this configuration, the electrodes function as conductive measurement terminals for pairwise resistance monitoring within the hydrogel sensor rather than as conventional bioelectrodes for biopotential recording. The hybrid ionic-electronic conduction mechanism of the hydrogel ensures minimal baseline resistance (~kΩ) and a high signal-to-noise ratio during minor forearm strain (~1–10% $\Delta R/R_0$). In addition, the flexible Cu-Ag contact helps maintain a stable electrical connection during dynamic gesturing (Figure 8B, Movie S2). The resistance variations measured across several electrode pairs organized in an 8×8 matrix are displayed as a normalized heat map in Figure 8C, in which each matrix represents the $\Delta R/R_0$ response for a given electrode pair. Darker hues indicate relatively larger normalized responses, whereas lighter hues indicate relatively smaller responses. Thus, the heat map provides a visual comparison of pair-dependent deformation responses across the sensing area rather than a direct quantitative strain distribution obtained from eight independent sensing units. We anticipate that our high-performance stress gauge will play a crucial role in future flexible electronics for use in everyday applications, thereby enabling continuous, long-term, and steady health monitoring.

4 | Conclusion

Herein, we reported an effective relationship between controlled plasticization and the durability of a hydrogel. Unlike conventional research that focuses on standard synthesis and characterization techniques, we created an optimal network by optimizing the solvent chemistry and modifying the structure of the hydrogel. The optimal water/glycerol concentration was found to afford a significantly lower curing time and less dehydration. In addition, the experimental outcomes unequivocally demonstrate the successful establishment of interactions between the structural matrix and functional additives that directly influence the mechanical and sensing characteristics of the hydrogel. Our comprehensive analysis of the dynamic hysteresis assessment methodology revealed minimal hystereses for stretch rates below 2%, which provides

26884062, 2026, 9, Downloaded from https://onlinelibrary.wiley.com/doi/10.1002/sstr.70619 by Hanyang University Library, Wiley Online Library on [19/10/2026]. See the Terms and Conditions (https://onlinelibrary.wiley.com/terms-and-conditions) on Wiley Online Library for rules of use; OA articles are governed by the applicable Creative Commons License

significant benefits for deformation-dependent sensors. This nearly perfect elastic recovery guarantees hysteresis-free linear electromechanical transduction and facilitates the precise recording of forearm extensor muscle dynamics during seamless finger movements. Hence, the superior electromechanical performance delivered using our approach is expected to motivate further research into the use of hydrogels across a number of fields under more rigorous operational conditions. We believe that these hydrogels will be extensively used in multipoint flexible sensors, modern soft robotics, and wireless wearable sensors, where materials are often exposed to numerous s–s cycles.

Author Contributions

Animesh Sinha: writing – original draft, visualization, investigation, conceptualization, data curation, formal analysis, methodology, and software. **Minjoon Kim:** investigation, conceptualization, data curation, and analysis. **Hongyun So:** writing – review and editing, supervision, resources, methodology, funding acquisition.

Funding

This research was supported by the ANCHOR through the Seoul ANCHOR Center, funded by the Ministry of Education (MOE) and the Seoul Metropolitan Government (2026-ANCHOR-01-027-04) and by the National Research Foundation of Korea (NRF), funded by the Ministry of Science and ICT of the Republic of Korea (No. RS-2023-00260527).

Conflicts of Interest

The authors declare no conflicts of interest.

Data Availability Statement

The datasets used and/or analyzed during the current study are available from the corresponding author on reasonable request.

References

1. K. S. Anseth, C. N. Bowman, and L. Brannon-Peppas, "Mechanical Properties of Hydrogels and Their Experimental Determination," *Biomaterials* 17 (1996): 1647–1657, https://doi.org/10.1016/0142-9612(96)87644-7.

2. J. Tang, J. Li, J. J. Vlassak, and Z. Suo, "Fatigue Fracture of Hydrogels," *Extreme Mechanics Letters* 10 (2017), 24–31, https://doi.org/10.1016/j.eml.2016.09.010.

3. R. Bai, J. Yang, X. P. Morelle, C. Yang, and Z. Suo, "Fatigue Fracture of Self-Recovery Hydrogels," *ACS Macro Letters* 7 (2018): 312–317, https://doi.org/10.1021/acsmacrolett.8b00045.

4. M. Nam, J. Chang, H. Kim, et al., "Highly Reliable and Stretchable OLEDs Based on Facile Patterning Method: Toward Stretchable Organic Optoelectronic Devices," *Npj Flexible Electronics* 8 (2024): 17, https://doi.org/10.1038/s41528-024-00303-5.

5. J. W. Li, C. Y. Huang, B. H. Zhou, et al., "High Stretchability and Conductive Stability of Flexible Hybrid Electronic Materials for Smart Clothing," *Chemical Engineering Journal Advances* 12 (2022): 100380, https://doi.org/10.1016/j.ceja.2022.100380.

6. S. He, Z. Liu, H. Fang, et al., "Flexible, Rapid Self-Healing and Ultra-Sensitive Hydrogel Sensor With Dynamic Multi-Interactions for Human Motion Detection," *European Polymer Journal* 222 (2025): 113612, https://doi.org/10.1016/j.eurpolymj.2024.113612.

7. H. Hu, D. Li, T. Salim, et al., "Electrically Driven Hydrogel Actuators: Working Principle, Material Design and Applications," *Journal of Materials Chemistry C* 12 (2024): 1565–1582, https://doi.org/10.1039/d3tc03863g.

8. A. López-Díaz, A. S. Vázquez, and E. Vázquez, "Hydrogels in Soft Robotics: Past, Present, and Future," *ACS Nano* 18 (2024): 20817–20826, https://doi.org/10.1021/acsnano.3c12200.

9. T. Dutta, P. Chaturvedi, I. Llamas-Garro, J. S. Velázquez-González, R. Dubey, and S. K. Mishra, "Smart Materials for Flexible Electronics and Devices: Hydrogel," *RSC Advances* 14 (2024): 12984–13004, https://doi.org/10.1039/d4ra01168f.

10. Y. Tian, Z. Wang, S. Cao, et al., "Connective Tissue Inspired Elastomer-Based Hydrogel for Artificial Skin via Radiation-Induced Penetrating Polymerization," *Nature Communications* 15 (2024): 636, https://doi.org/10.1038/s41467-024-44949-1.

11. K. Zöller, D. To, and A. Bernkop-Schnürch, "Biomedical Applications of Functional Hydrogels: Innovative Developments, Relevant Clinical Trials and Advanced Products," *Biomaterials* 312 (2025): 122718, https://doi.org/10.1016/j.biomaterials.2024.122718.

12. A. Ahmed, W. Xian, M. F. Hassan, et al., "Strong, Tough, and Dynamically Reversible Hydrogels Enabled by a Freeze–thawing, Densification, and Crosslinking Strategy," *Materials Today* 93 (2026): 103185, https://doi.org/10.1016/j.mattod.2026.01.006.

13. B. S. Chee, G. Goetten de Lima, D. M. Devine, and M. J. D. Nugent, "Investigation of the Effects of Orientation on Freeze/Thawed Polyvinyl Alcohol Hydrogel Properties," *Materials Today Communications* 17 (2018), 82–93, https://doi.org/10.1016/j.mtcomm.2018.08.005.

14. X. Qi, X. Hu, W. Wei, et al., "Investigation of Salecan/Poly(vinyl Alcohol) Hydrogels Prepared by Freeze/Thaw Method," *Carbohydrate Polymers* 118 (2015): 60, https://doi.org/10.1016/j.carbpol.2014.11.021.

15. W. Yang, J. Zhou, Q. Yang, T. Qiu, and S. Yu, "Dual-Enhanced Hydrogel Actuators Enabled by Tuning the Polymer Network Through Synergistic CNT-Dynamic Covalent Bonds," *Composites Science and Technology* 277 (2026): 111539, https://doi.org/10.1016/j.compscitech.2026.111539.

16. H. Adelnia, R. Ensandoost, S. Shebbrin Moonshi, J. N. Gavgani, E. I. Vasafi, and H. T. Ta, "Freeze/Thawed Polyvinyl Alcohol Hydrogels: Present, Past and Future," *European Polymer Journal* 164 (2022): 110974, https://doi.org/10.1016/j.eurpolymj.2021.110974.

17. J. Kang, B. Wu, S. Chen, et al., "Solvent-Induced Biphasic Phase Separated Hydrogels: Synergistic Energy Dissipation for Softness, Ultra-Tough and Shape Recovery," *Chemical Engineering Journal* 529 (2026): 172732, https://doi.org/10.1016/j.cej.2026.172732.

18. M. Dong, Y. Sun, G. Wang, et al., "Temperature-Triggered Adhesiveness-Controllable Ionic-Conductive Hydrogels for Wearable Electronic Applications," *Applied Materials Today* 48 (2026): 103053, https://doi.org/10.1016/j.apmt.2025.103053.

19. Y. Li, Y. Zhang, B. Chang, et al., "Piezoionic Effect in Gels: Multifunctional Applications From Energy Harvesting to Intelligent Sensing," *Nanoscale* 18 (2026): 3472–3495, https://doi.org/10.1039/d5nr04389a.

20. Z. Zhang, Y. Mu, L. Xiao, et al., "Hydrogel Electrolytes for Zinc-Ion Batteries: Materials Design, Functional Strategies, and Future Perspectives," *Nano-Micro Lett* 18 (2026): 139, https://doi.org/10.1007/s40820-025-01993-w.

21. T. Zhou, H. Li, J. Mao, Z. Yi, H. Hua, and A. Zhu, "Multifunctional Conductive Hydrogels: Design Strategies and Applications in Wearable Sensors and Flexible Supercapacitors," *Small* 22 (2026): e12674, https://doi.org/10.1002/smll.202512674.

22. D. Luo, L. Yang, Z. Geng, et al., "Underlying Principles and Practical Design Strategies of Hydrogel Electrolytes for Long-Term Stable Zinc Batteries," *Advanced Energy Materials* 16 (2026): e04151, https://doi.org/10.1002/aenm.202504151.

26884062, 2026, 9, Downloaded from https://onlinelibrary.wiley.com/doi/10.1002/sstr.70619 by Hanyang University Library, Wiley Online Library on [19/10/2026]. See the Terms and Conditions (https://onlinelibrary.wiley.com/terms-and-conditions) on Wiley Online Library for rules of use; OA articles are governed by the applicable Creative Commons License

23. M. Y. Lee, E. S. Lee, N. Y. Ko, et al., "Emerging Roles of Hydrogels, Organogels, and Their Hybrids in Soft Bioelectronics and Bioplatforms," *Npj Biosens* 2 (2025): 35, https://doi.org/10.1038/s44328-025-00055-w.

24. E. Zhang, R. Bai, X. P. Morelle, and Z. Suo, "Fatigue Fracture of Nearly Elastic Hydrogels," *Soft Matter* 14 (2018): 3563–3571, https://doi.org/10.1039/c8sm00460a.

25. D. Sun, Y. Gao, Y. Zhou, et al., "Enhance Fracture Toughness and Fatigue Resistance of Hydrogels by Reversible Alignment of Nanofibers," *ACS Applied Materials & Interfaces* 14 (2022): 49389–49397, https://doi.org/10.1021/acsami.2c16273.

26. H. Lei, L. Dong, Y. Li, et al., "Stretchable Hydrogels With Low Hysteresis and Anti-Fatigue Fracture Based on Polyprotein Cross-Linkers," *Nature Communications* 11 (2020): 4032, https://doi.org/10.1038/s41467-020-17877-z.

27. X. Liang, G. Chen, S. Lin, et al., "Anisotropically Fatigue-Resistant Hydrogels," *Advanced Materials* 33 (2021): 2102011, https://doi.org/10.1002/adma.202102011.

28. Z. Shen, Z. Zhang, N. Zhang, et al., "High-Stretchability, Ultralow-Hysteresis Conducting Polymer Hydrogel Strain Sensors for Soft Machines," *Advanced Materials* 34 (2022): 2203650, https://doi.org/10.1002/adma.202203650.

29. Z. Zhang, G. Chen, Y. Xue, et al., "Fatigue-Resistant Conducting Polymer Hydrogels as Strain Sensor for Underwater Robotics," *Advanced Functional Materials* 33 (2023): 2305705, https://doi.org/10.1002/adfm.202305705.

30. J. Yu, R. Wan, F. Tian, et al., "3D Printing of Robust High-Performance Conducting Polymer Hydrogel-Based Electrical Bioadhesive Interface for Soft Bioelectronics," *Small* 20 (2024): 2308778, https://doi.org/10.1002/smll.202308778.

31. L. Wang, W. Chen, H. Li, et al., "Ultrasoft, Anti-Dehydrated, and Highly Stretchable Carboxymethylcellulose-Based Organohydrogel Strain Sensors for Non-Invasive Real-Time Plant Growth Monitoring," *Carbohydrate Polymers* 364 (2025): 123753, https://doi.org/10.1016/j.carbpol.2025.123753.

32. X. Y. Xue, L. Han, H. Q. Cai, et al., "Conductive Hydrogel-Based Neural Interfaces: From Fabrication Methods, Properties, to Applications," *Small Structures* 6 (2025): 2400696, https://doi.org/10.1002/sstr.202400696.

33. L. Lu, X. Chen, Y. Zhang, et al., "Bioinspired Ion-Proton Bipathway All-Natural Hydrogel With Enhanced Conductivity for Bioelectronic Interfaces," *Advanced Functional Materials* 36 (2026): e76841, https://doi.org/10.1002/adfm.76841.

34. P. Zhu, Y. Zhang, A. Wu, et al., "A Damping and Adhesive Hydrogel Electrode for Continuous High-Fidelity Dynamic Electrophysiological Monitoring and Human–machine Interaction," *Nano Research* 19 (2026): 94908565, https://doi.org/10.26599/NR.2026.94908565.

35. B. Chen, R. Yu, J. Wang, et al., "Biomaterials-Based Hydrogel With Superior Bio-Mimetic Ionic Conductivity and Tissue-Matching Softness for Bioelectronics," *Advanced Functional Materials* 36 (2026): e27495, https://doi.org/10.1002/adfm.202527495.

36. B. Liu, T. Yin, J. Zhu, et al., "Tough and Fatigue-Resistant Polymer Networks by Crack Tip Softening," *Proceedings of the National Academy of Sciences of the United States of America* 120 (2023): e2217781120, https://doi.org/10.1073/pnas.2217781120.

37. J. Kim, G. Zhang, M. Shi, and Z. Suo, "Fracture, Fatigue, and Friction of Polymers in which Entanglements Greatly Outnumber Cross-Links," *Science* 374 (2021): 212, https://doi.org/10.1126/science.abg6320.

38. Z. Huang, J. Peng, W. Zhang, K. Yue, and X. Wang, "Ultra-Stretchable and Crack-Resistant Nonpolar Organogels," *Nature Communications* 17 (2026): 2045, https://doi.org/10.1038/s41467-026-68775-9.

39. Y. He, H. K. Tsao, and S. Jiang, "Improved Mechanical Properties of Zwitterionic Hydrogels With Hydroxyl Groups," *Journal of Physical Chemistry B* 116 (2012): 5766, https://doi.org/10.1021/jp300205m.

40. Q. Zhou, J. Lyu, G. Wang, et al., "Mechanically Strong and Multifunctional Hybrid Hydrogels With Ultrahigh Electrical Conductivity," *Advanced Functional Materials* 31 (2021): 2104536, https://doi.org/10.1002/adfm.202104536.

41. M. Kang, O. Oderinde, X. Han, G. Fu, and Z. Zhang, "Development of Oxidized Hydroxyethyl Cellulose-Based Hydrogel Enabling Unique Mechanical, Transparent and Photochromic Properties for Contact Lenses," *International Journal of Biological Macromolecules* 183 (2021): 1162, https://doi.org/10.1016/j.ijbiomac.2021.05.029.

42. J. Zhou, S. Lin, H. Zeng, et al., "Dynamic Intermolecular Interactions Through Hydrogen Bonding of Water Promote Heat Conduction in Hydrogels," *Materials Horizons* 7 (2020): 2936–2943, https://doi.org/10.1039/d0mh00735h.

43. D. T. Tadele, D. David, E. Yim, and T. H. Mekonnen, "Development and Characterization of PVA-Zein/α-Tocopherol Nonwoven Mats for Functional Wound Dressing Applications," *Colloids and Surfaces B: Biointerfaces* 246 (2025): 114355, https://doi.org/10.1016/j.colsurfb.2024.114355.

44. Y. Xu, P. Liu, and Y. Zhang, "Mid-Infrared Spectroscopy of Hemispherical Water Droplets," *Spectrochimica Acta Part A: Molecular and Biomolecular Spectroscopy* 264 (2022): 120256, https://doi.org/10.1016/j.saa.2021.120256.

45. A. Jarosz, O. Kapusta, D. Gugała-Fekner, and M. Barczak, "Synthesis and Characterization of Agarose Hydrogels for Release of Diclofenac Sodium," *Materials* 16 (2023): 6042, https://doi.org/10.3390/ma16176042.

46. A. M. Atta, A. A. Melegy, and A. N. El-hoshoudy, "New Recycled Polyethylene Terephthalate Imidazolium Ionic Liquids and Their Applications for CO_2 Exhaust Capture," *Scientific Reports* 15 (2025): 30378, https://doi.org/10.1038/s41598-025-15433-7.

47. K. Thakur, A. Rajhans, and B. Kandasubramanian, "Starch/PVA Hydrogels for Oil/Water Separation," *Environmental Science and Pollution Research* 26 (2019): 32013–32028, https://doi.org/10.1007/s11356-019-06327-z.

48. G. Al Boustani, L. Bichlmaier, T. F. Teshima, et al., "Flexible Conductive Paper-Based Sensors for on-Skin Electrophysiological Monitoring and Wearable Applications," *ACS Applied Materials & Interfaces* 18 (2025): 989, https://doi.org/10.1021/acsami.5c22432.

49. P. Zhu and Z. Zhong, "Analysis of the Mullins Effect in Buckling Instability of Double-Network Hydrogel Beams Under Swelling Equilibrium," *International Journal of Solids and Structures* 288 (2024): 112627, https://doi.org/10.1016/j.ijsolstr.2023.112627.

50. M. Uchida, T. Sengoku, Y. Kaneko, D. Okumura, H. Tanaka, and S. Ida, "Evaluation of the Effects of Cross-Linking and Swelling on the Mechanical Behaviors of Hydrogels Using the Digital Image Correlation Method," *Soft Matter* 15 (2019): 3389–3396, https://doi.org/10.1039/c9sm00049f.

51. T. Liu, X. B. Wang, F. Y. Sun, et al., "Multiscale Interlinked Structures Limit Fatigue Crack Propagation in a MXene-Polyurethane Composite," *Nature Communications* 16 (2025): 9555, https://doi.org/10.1038/s41467-025-64611-8.

52. W. Zhang, J. Hu, J. Tang, et al., "Fracture Toughness and Fatigue Threshold of Tough Hydrogels," *ACS Macro Letters* 8 (2019): 17–23, https://doi.org/10.1021/acsmacrolett.8b00788.

53. L. Liu, D. Zhang, P. Bai, et al., "Fatigue-Resistant and Super-Tough Thermocells," *Nature Communications* 16 (2025): 1963, https://doi.org/10.1038/s41467-025-57233-7.

54. J. Wu, J. Zhang, Y. Chen, W. Ji, Q. Wu, and L. Guan, "Fatigue-Resistant Hydrogels With Programmable Crystalline Domain Crosslinking Enabled by Coordinated Thermal-Solvent Strategy," *Journal of Materials Chemistry A* 13 (2025): 29006–29015, https://doi.org/10.1039/d5ta05010c.

55. E. K. Boahen, Z. Kong, S. Y. Kim, et al., "Autonomous Polymer Frameworks for Sustainable Tissue-Interfaced Plastic Bioelectronics,"

26884062, 2026, 9, Downloaded from https://onlinelibrary.wiley.com/doi/10.1002/sstr.70619 by Hanyang University Library, Wiley Online Library on [19/10/2026]. See the Terms and Conditions (https://onlinelibrary.wiley.com/terms-and-conditions) on Wiley Online Library for rules of use; OA articles are governed by the applicable Creative Commons License

Advancement of Science 13 (2026): e15320, https://doi.org/10.1002/advs.202515320.

56. C. Xue, X. Qiu, Z. Zhang, et al., "Design, Fabrication, and Applications of Bioinspired Strong and Tough Hydrogels," *Advanced Materials Technologies* 11 (2026): e02128, https://doi.org/10.1002/admt.202502128.

57. Z. Xie, L. Yuan, X. Qing, Y. Wang, X. Wu, and X. Weng, "Hygroscopic Mg–Al LDHs Composite Microspheres for Highly Efficient Hyperspectral Camouflage in the VIS and NIR Wavebands," *Scientific Reports* 14 (2024): 15649, https://doi.org/10.1038/s41598-024-66538-4.

58. Z. Huang, M. Lyu, N. Meng, J. Cao, C. Xiong, and F. Lian, "Electrically Conductive Functional Polymers and Application Progress in Lithium Batteries," *Polymers* 17 (2025): 778, https://doi.org/10.3390/polym17060778.

Supporting Information

Additional supporting information can be found online in the Supporting Information section.

26884062, 2026, 9, Downloaded from https://onlinelibrary.wiley.com/doi/10.1002/sstr.70619 by Hanyang University Library, Wiley Online Library on [19/10/2026]. See the Terms and Conditions (https://onlinelibrary.wiley.com/terms-and-conditions) on Wiley Online Library for rules of use; OA articles are governed by the applicable Creative Commons License